Click Here for Full Article

Saturn kilometric radiation: Average and statistical properties

L. Lamy,[1] P. Zarka,[1] B. Cecconi,[1] R. Prangé,[1] W. S. Kurth,[2] and D. A. Gurnett[2]

[1]   Since Cassini entered Saturn's magnetosphere in July 2004, the auroral Saturnian kilometric radiation (SKR), which dominates the kronian radio spectrum, is observed quasi-continuously. Consecutive orbits of the spacecraft covered distances to Saturn down to 1.3 Saturn radii, all local times and, since December 2006, latitudes as high as 60°. On the basis of carefully calibrated and cleaned long-term time series and dynamic spectra, we analyze the average properties, and characteristics of the SKR over 2.75 years starting at Cassini's Saturn orbit insertion. This study confirms and expands previous results from Voyager 1 and 2 studies in the 1980s: the SKR spectrum is found to extend from a few kHz to 1200 kHz; extraordinary mode emission dominates, i.e., left-handed (LH) from the southern kronian hemisphere and right-handed (RH) from the northern one, for which we measure directly a degree of circular polarization up to 100%; the variable visibility of SKR along Cassini's orbit is consistent with sources at or close to the local electron cyclotron frequency f_{ce}, in the Local Time (LT) sector 09 h–12 h, and at latitudes $\geq 70°$, with emission beamed along hollow cones centered on the local magnetic field vector; this anisotropic beaming results in the existence of an equatorial radio shadow zone, whose extent is quantified as a function of frequency; it also causes the systematic disappearance of emission at high latitudes above 200 kHz and below 30 kHz. In addition, we obtain new results on SKR: LH and RH intensity variations are found to match together at all timescales ≥ 30 min; moreover their spectra are found to be conjugated as a function of the latitude of the observer; we use this conjugacy to merge LH and RH spectra and derive pronounced systematic dependences of the SKR spectrum as a function of the spacecraft latitude and LT (that will be the input of a subsequent modeling study); we identify for the first time ordinary mode SKR emission; finally, in addition to the SKR and n-SMR components, we discuss the narrowband kilometric component (named here n-SKR) which extends mainly between 10 and 40 kHz, preferentially observed from high latitudes.

1. Introduction

[2]   The nonthermal auroral Saturnian kilometric radiation (hereafter SKR) is the most intense radio emission from Saturn and presents strong similarities with the Earth's auroral kilometric radiation (AKR) and Jovian auroral radio emissions (broadband kilometer, hectometer, and Io-independent decameter emissions) [*Zarka*, 1998]. SKR was discovered by the Voyager 1 planetary radio experiment in January 1980 [*Kaiser et al.*, 1980]. Its name refers to the characteristic wavelength of the emission, i.e., a typical frequency range from about 3 kHz to 1.2 MHz, peaking between 100 and 400 kHz. SKR is strongly circularly polarized, and the Voyagers have detected two SKR components with opposite senses of polarization: a right-handed (RH) component originating from the northern hemisphere and a left-handed (LH) one from the southern hemisphere, consistent with emission on the extraordinary mode [*Kaiser et al.*, 1980, 1984; *Warwick et al.*, 1982].

[3]   Analyses of Voyager observations showed that SKR sources do not corotate with the planet but are rather restricted in local time (LT) in the morning-to-noon sector, and located at high latitudes [*Warwick et al.*, 1981; *Lecacheux and Genova*, 1983; *Galopeau et al.*, 1995].

[4]   As similar radio emissions from other planets, SKR is thus believed to be generated by accelerated electron beams in the auroral zones via the cyclotron maser instability, which favors extraordinary mode emission near the local electron cyclotron frequency f_{ce} at the source [*Galopeau et al.*, 1989; *Zarka*, 1998]. The theory predicts that the emission is beamed along hollow cones whose axis is

[1]LESIA, Observatoire de Paris, CNRS, UPMC, Université Paris Diderot, Meudon, France.
[2]Department of Physics and Astronomy, University of Iowa, Iowa City, Iowa, USA.
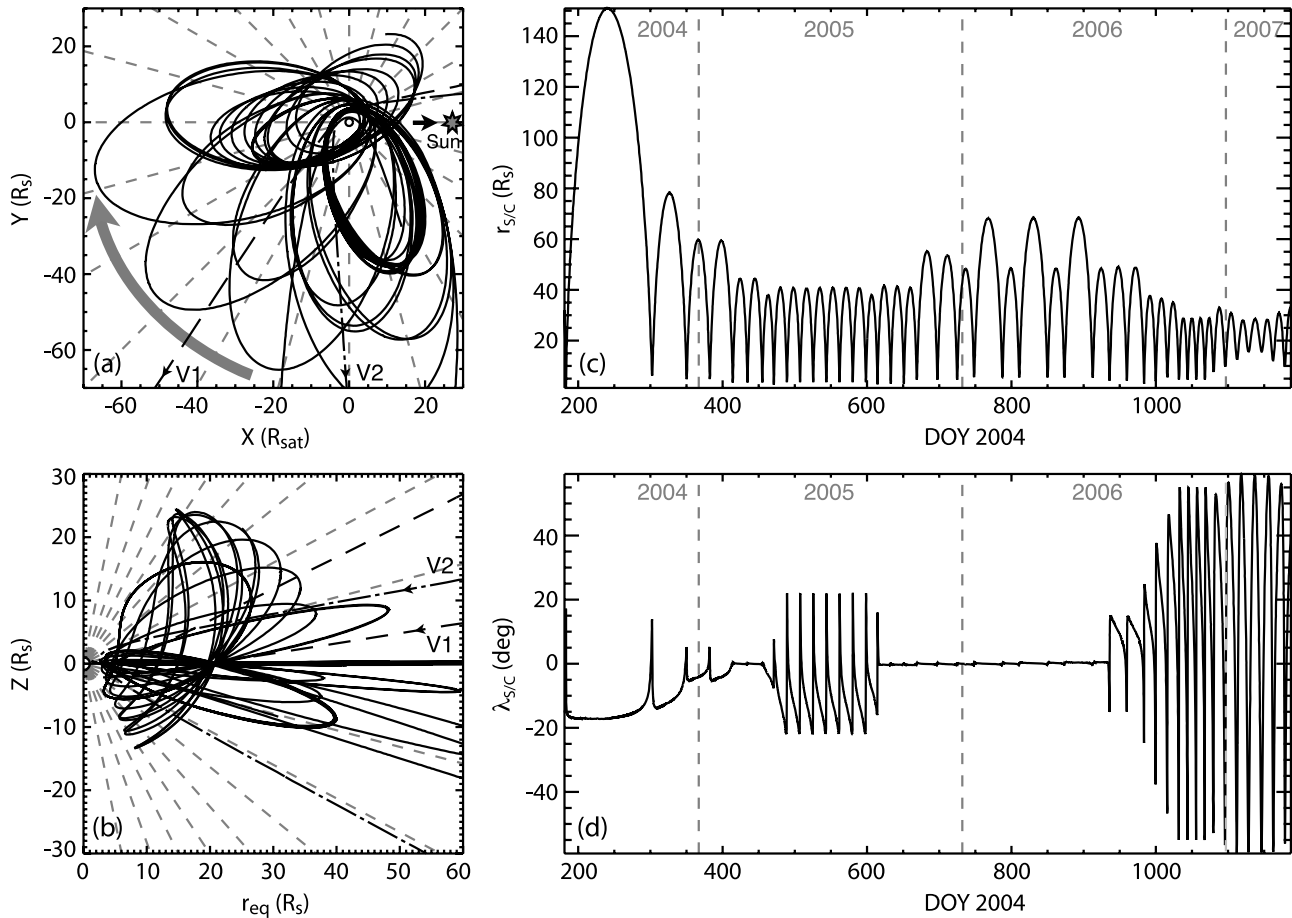
Figure 1. Ephemeris of the Cassini spacecraft between day 181 and 1186 of year 2004. We use a system of equatorial coordinates centered on Saturn: the x axis points toward the Sun, the z axis is aligned with the rotation axis of the planet and the y axis completes the frame. Dashed and dash-dotted black lines indicate the trajectories of Voyager 1 (in 1980) and 2 (in 1981). (a) Consecutive orbits in the equatorial plane. Their precession is indicated by the grey arrow. The dashed grey lines mark 1 h steps in local time with noon LT indicated by the black arrow pointing at the Sun. (b) The spacecraft trajectory cylindrically projected onto a meridian plane. $r_{eq} = \sqrt{x^2 + y^2}$ is the distance of Cassini from Saturn in the equatorial plane and z is the altitude above this plane. The dashed grey lines mark 10° steps in latitude. (c and d) The spacecraft distance to Saturn $r_{sc} = \sqrt{x^2 + y^2 + z^2}$ and latitude λ_{sc} as a function of time.

aligned with the local magnetic field at the source. This implies strong variations of visibility of the emission as a function of the observer's position around the planet. Before Cassini, SKR was studied only using the two Voyagers and the Ulysses spacecraft. The Voyagers discovered SKR and measured some of its basic properties during their flybys of Saturn, but their observations were restricted to three positions in LT and limited latitude range. SKR detection by Ulysses was at too low signal-to-noise (SNR) ratio for addressing properties other than those related to its occurrence, as its rotational modulation [*Galopeau and Lecacheux*, 2000].

[5] Cassini has been orbiting Saturn since July 2004 and the Radio Plasma and Wave Science (RPWS) instrument [*Gurnett et al.*, 2004] has observed SKR from all LT and a broad range of latitudes. Following *Zarka et al.* [2004] and *Cecconi and Zarka* [2005], we calibrated the nearly continuous RPWS data and derived the intensity and circular polarization state of observed radio waves as a function of

time and frequency. These physical parameters are analyzed here to determine SKR average and statistical properties and put further constraints on sources location and emission beaming.

[6] In this paper, we address some open questions concerning the SKR. What are the main characteristics of the SKR spectrum and polarization? Are there differences between LH and RH spectra? Do these components exhibit the same temporal variations? How does SKR vary with the observer's position (local time, latitude), and how does this translate to constraints on models? Can we find evidence for new low frequency (LF) components or O-mode emission? In section 2, we briefly describe Cassini's trajectory, the RPWS radio receiver, and the 2.75 years data set analyzed here. Section 3 deals with the general phenomenology of dynamic spectra of Saturn's kilometric emissions, including the identification of a new component. We analyze the SKR polarization and emission modes in section 4. Section 5 investigates the SKR beaming and the disappearance
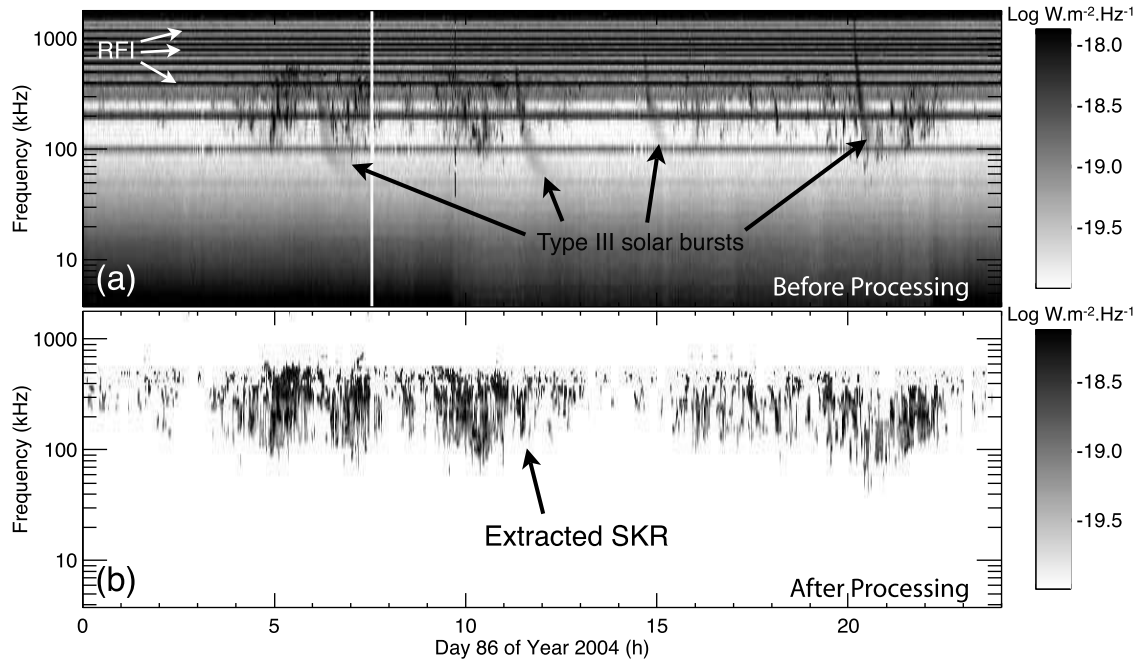
Figure 2. (a) Raw dynamic spectrum recorded by Cassini-RPWS/HFR on DOY 86, ∼800 R$_s$ away from Saturn. (b) SKR flux density S extracted by our processing.

observed at low and high latitudes. In section 6 we derive average and peak SKR spectra for both polarizations and several latitude ranges, as well as average and peak emitted powers. Section 7 compares the temporal variations of LH and RH SKR components. Finally, section 8 shows the clear conjugacy between LH and RH spectra as a function of observer's latitude, allowing to further address SKR visibility as a function of the LT and latitude of Cassini and identify O-mode SKR emission. The constraints brought by these results on sources localization, beaming and dynamics will be the subject of a follow-on paper based on the modeling of SKR visibility along Cassini's orbit.

2. Observations

2.1. Ephemeris

[7] The data discussed here cover a time interval of 1006 days (2.75 years) from day 181 of year 2004 (2 days before Saturn Orbit Insertion (SOI) of Cassini) to day 90 of year 2007. We will hereafter express time in days of year 2004 (noted DOY) with a reference set on 1 January, of year 2004. During this 2.75 years interval, the spacecraft performed 42 orbits around Saturn and spent ∼60% of the time in the southern hemisphere. This implies differences in the conditions of observation of each hemisphere. Figure 1 displays the relevant parameters of Cassini's trajectory.

[8] The consecutive perikrones precess from ∼20 h to ∼12 h LT, as displayed on Figure 1a (spacecraft local time will be noted LT$_{sc}$). This uneven sampling and the large orbital eccentricity implies that different amounts of time are spent at different LT$_{sc}$. A broad latitude range ($-60° \leq \lambda_{sc} \leq +60°$) has been swept by Cassini (Figures 1b and 1d), with near-equatorial orbits between DOY 620 and 930 and high latitude excursions thereafter. The distance from

Cassini to Saturn r_{sc} varies from 1.33 Saturn radii (R$_s$) at SOI to a maximum distance of 151 R$_s$ (Figure 1c).

2.2. Instrument and Data

[9] Cassini-RPWS includes a High Frequency Receiver (HFR) which measures the wave electric field along three electric monopole antennas $\mathbf{h}_{+x}$, $\mathbf{h}_{-x}$, and $\mathbf{h}_z$ (also noted $\mathbf{h}_u$, $\mathbf{h}_v$, and $\mathbf{h}_w$) or the virtual dipole $\mathbf{h}_x$ formed by the pair ($\mathbf{h}_{+x}$, $\mathbf{h}_{-x}$), over the range 3.5 kHz to 16.125 MHz [*Gurnett et al.*, 2004]. The effective lengths of electrical antennas are 1.68 m for the monopoles and 3.06 m for the dipole [*Zarka et al.*, 2004]. The receiver computes auto- and cross-correlations of antenna signals from which goniopolarimetric inversions [*Cecconi and Zarka*, 2005] allow us to extract the wave parameters: flux and polarization state (known as Stokes parameters [*Kraus*, 1966]), and direction of arrival (**k**-vector). The HFR operates in several modes with various temporal and spectral resolutions resulting in a very inhomogeneous data set on the long term.

[10] In order to study SKR, we built calibrated, cleaned and homogeneous long-term time series and dynamic spectra of received flux densities (in $W{\cdot}m^{-2}{\cdot}Hz^{-1}$) normalized to 1 AU, emitted powers (in $W{\cdot}sr^{-1}$), and normalized circular polarization degrees, over the 2.75 years period studied.

[11] The specific data processing pipeline is described in details in the Appendix. As an example, Figure 2 illustrates the "cleaning" step of the processing: in addition to SKR, Figure 2a includes solar type III bursts and radio frequency interference (RFI). After processing (Figure 2b), SKR only has been automatically extracted. Processed data are finally rebinned over the whole period with a constant time resolution of 180 s per spectrum in frequency bins consisting of 24 logarithmically spaced channels between 3.5 and

300 kHz (with $\Delta f/f = 20\%$) and 24 linearly spaced channels (with $\delta f = 50$ kHz) between 350 and 1500 kHz.

3. Saturn's Low Frequency Radio Components

[12] Figure 3 is an overview of Saturn's emissions detected in the kilometer range. Each double panel (a, b, c, d) displays a dynamic spectrum of the normalized flux density S (with subscript 1) and a dynamic spectrum of the normalized degree of circular polarization V (with subscript 2). V = 1 corresponds to pure LH circularly polarized emission, and V = −1 to pure RH one. Figure 3a displays the full data set over 2.75 years. SKR extends from ~10 to ~1000 kHz. Additional LF emissions show up after DOY 550 between 3 and 40 kHz. Figure 3a$_2$ illustrates the good correspondence between the latitude of Cassini and the observed circular polarization, revealing the hemisphere of origin of the emission. During the first orbits (DOY 181 to 400) as well as during medium latitude excursions (DOY 470 to 620), Cassini spent most of the time in the southern hemisphere. The observed dominant polarization is LH (displayed in black on Figure 3a), consistent with emission on the extraordinary mode (see section 4), whereas RH was only observed during short intervals spent in the northern hemisphere. High latitude excursions (after DOY 930) illustrate the opposite situation with most of the time spent in the north. During near-equatorial orbits (DOY 400 to 470, and DOY 620 to 930), emissions from both hemispheres are detected simultaneously, resulting in apparent circular polarization weaker than that measured at higher λ_{sc}. However, LH polarization still predominates, except at high frequencies (≥ 600 kHz) where the RH component takes over. These points are discussed in sections 6 and 7.

[13] Figure 3b focuses on typical observations from low λ_{sc}: SKR is prominent above 20 kHz, but emissions below 20 kHz episodically appear. These LF emissions are weakly polarized and include local electrostatic and electromagnetic emissions observed near perikrones, as well as a few spurious emissions.

[14] Figure 3c displays typical observations from high latitude passes. The periodic motion of the spacecraft across each hemisphere is clearly visible in Figure 3c$_2$ as the alternance of the dominant circular polarization detected. In addition to SKR, other circularly polarized but less intense components appear below 40 kHz. They are better visible on Figure 3d which zooms on an interval of 12 d including high latitude excursions at $\lambda_{sc} = -52.82°$ (on DOY 1079) and $\lambda_{sc} = +52.82°$ (on DOY 1083). We identify here three distinct components: (1) SKR extends from 3.5 to 1200 kHz. It is intense and highly circularly polarized. We notice that its frequency range increases with $|\lambda_{sc}|$ but

shrinks, especially at high frequencies, for $\lambda_{sc} \geq 55°$ (e.g., between DOY 1082 and 1085). (2) An intense but weakly circularly polarized emission shows up below 10 kHz. It has been named n-SMR (for narrowband Saturnian Myriametric Radiation) by *Louarn et al.* [2007]. (3) In addition, we identify a third component in the range 10–40 kHz, sometimes extending down to 3 kHz. This relatively narrowband emission corresponds – as n-SMR - to the narrowband electromagnetic emissions first reported by *Gurnett et al.* [1981]. It is less intense than SKR and n-SMR, and peaks about 20 kHz. It displays a high degree of circular polarization whose sign changes with the observer's hemisphere in opposition to that of SKR. Toward its high frequency end (30–40 kHz), the emission displays the same polarization as SKR. Although this could simply be the lowest frequency end of SKR, frequency-time connexity rather suggests that it is the upper frequency part of this new component, whose polarization is opposite to that of its lower part. Like n-SMR, this emission is modulated at or close to the SKR rotational periodicity [see *Zarka et al.*, 2007]. Further studies is needed to understand the origin of this component. Because of its spectral extent, intensity and polarization differ from n-SMR and since it belongs to the low frequency part of the SKR spectral range, we will call this component «n-SKR» in the rest of this paper. Hereafter we focus on the main, broadband SKR.

4. SKR Polarization

[15] SKR is thought to be emitted via the Cyclotron Maser Instability (CMI) [*Wu and Lee*, 1979; *Galopeau et al.*, 1989]. When the plasma in the source is depleted enough ($\epsilon_c = \frac{f_{pe}^2}{f_{ce}^2} \ll 1$), extraordinary (X) mode is predominantly generated, close to its LF cutoff frequency f_X, itself close to the local electron gyrofrequency f_{ce} [see *Le Quéau et al.*, 1985; *Hilgers*, 1992]. Near its LF cutoff, X mode is purely RH circularly polarized (R-X) with respect to the local magnetic field. SKR can also be produced on the ordinary (O) mode, with purely LH polarization (L-O), down to the O mode cutoff at the local electron plasma frequency f_{pe}, i.e., well below f_{ce}. We are interested only in R-X and L-O which are the free space modes. According to studies of Earth's AKR, L-O mode can be produced directly [*Treumann*, 2000] or via mode conversion [*Louarn and Le Quéau*, 1996a, 1996b; *Mutel et al.*, 2007], leading in both cases to intensities much lower than those of the R-X mode. R-X mode emissions from sources in the southern (resp. northern) hemisphere correspond to observed LH (resp. RH) circular polarization. The situation is opposite for L-O mode. The emission pattern resulting from the CMI is anisotropic: it consists of a widely open hollow cone whose

Figure 3. Dynamic spectra of flux density S normalized to 1 AU (subscript 1) and corresponding normalized degree of circular polarization V (subscript 2), displayed according to the grey scale bar on the right-hand side of each panel. (a) The entire interval studied from DOY 181 to 1186. Dynamic spectrum a$_2$ shows that the dominant circular polarization (black for LH, white for RH) alternates with λ_{sc}: LH (RH) component is preferentially observed when Cassini is located in the southern (northern) hemisphere. (b) Interval corresponding to near-equatorial orbits (DOY 700 to 800). LH polarization predominates on dynamic spectrum b$_2$ below 600 kHz, whereas RH polarization is more intense above that frequency. Figure 3c zooms on high latitude orbits, between DOY 1060 and 1186. Both polarizations are observed alternatively, following the alternance of λ_{sc}. (d) Subinterval of Figure 3c from DOY 1078 to 1090. In addition to intense broadband SKR, LF emissions show up below 40 kHz.
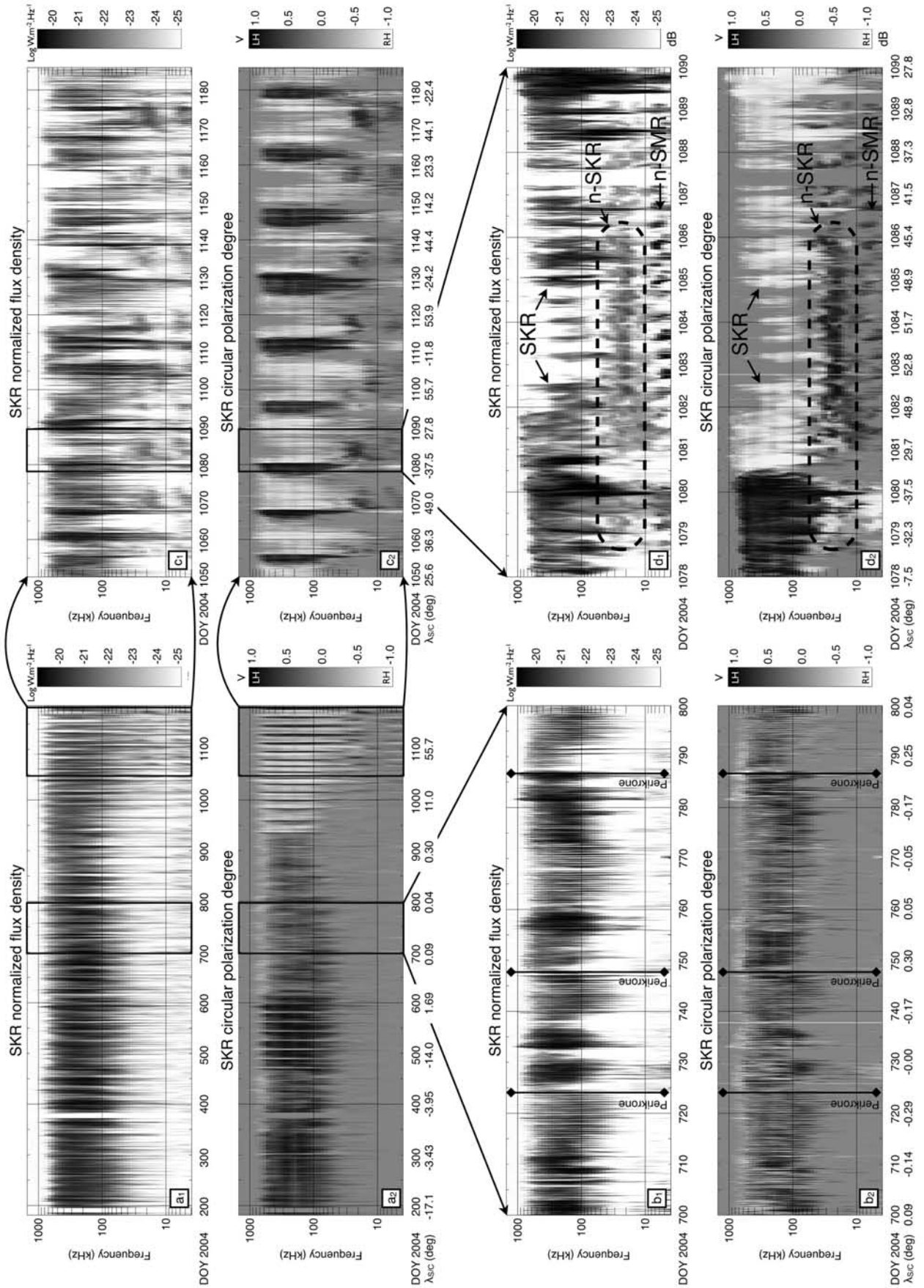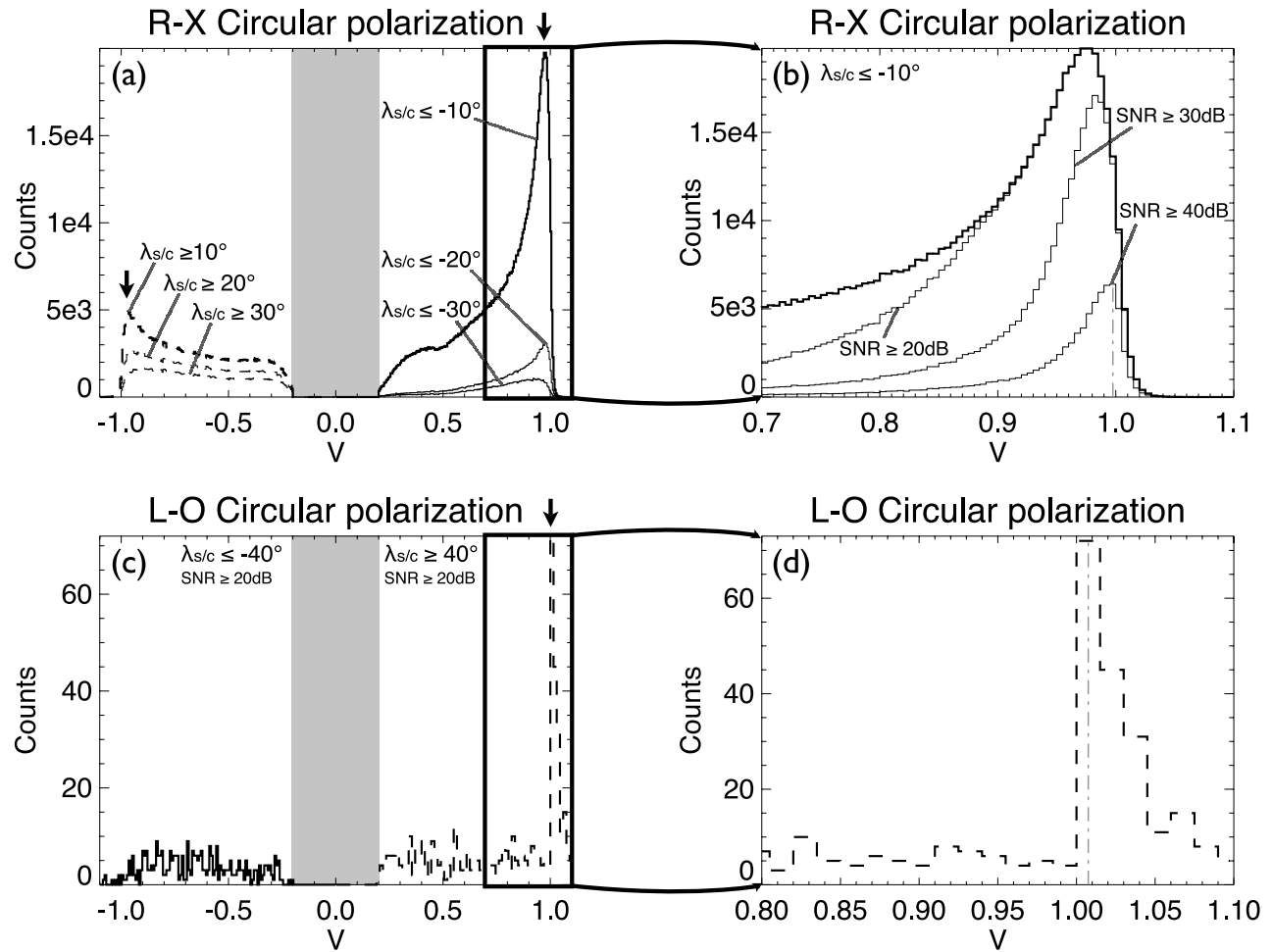
Figure 3

Figure 4. Histograms of SKR circular polarization degree V in the range [100,400 kHz] for high latitude excursions of the spacecraft. (a) LH polarization measured for emissions detected when $\lambda_{sc} \leq -10, -20,$ or $-30°$ (solid lines), and RH polarization measured for emissions detected when $\lambda_{sc} \geq 10, 20,$ or $30°$ (dashed lines). (b) Zoom of the LH histogram corresponding to $\lambda_{sc} \leq -10°$ (boldface) and similar LH histograms where an SNR threshold is imposed at 20, 30, and 40 dB (lightface). The distribution corresponding to SNR $\geq$ 40 dB peaks at 0.99 ± 0.01. (c) LH polarization measured for emissions detected when $\lambda_{sc} \geq 40°$ and SNR $\geq$ 20 dB (dashed line), and RH polarization measured for emissions detected when $\lambda_{sc} \leq -40°$ and SNR $\geq$ 20 dB (solid line). (d) Zoom of the LH histogram. A peak at 1.00 ± 0.01 is observed.

axis is along the local magnetic field; its aperture angle (also called beaming angle) depends on the local plasma parameters but cannot exceed 90°.

[16] Voyager studies [*Ortega-Molina and Lecacheux*, 1990] and the analysis of pre-SOI Cassini-RPWS/HFR data [*Cecconi et al.*, 2006] suggested that SKR has strong circular polarization. RPWS/HFR goniopolarimetric measurements can provide quasi-instantaneous measurements of the polarization state of incoming radio waves, allowing us to confirm and precise our knowledge of SKR polarization.

[17] Figure 4 displays our measured distribution of Stokes parameter V over the peak part of the SKR spectrum, between 100 and 400 kHz, restricted to time intervals corresponding to high latitude excursions of Cassini, in order to remove most of data points containing mixed emissions from both hemispheres. The grey shaded gap between V = −0.2 and V = +0.2 results from the elimination

of weakly polarized pixels in the process of SKR extraction (see Appendix).

[18] Figure 4a shows the distributions of SKR circular polarization ratio V for emissions whose sense of polarization and hemisphere of origin are compatible with R-X mode. The right part of the figure (solid lines) corresponds to LH emissions observed from $\lambda_{sc} \leq -10, -20,$ or $-30°$, while the left part (dashed lines) corresponds to RH emissions observed from $\lambda_{sc} \geq +10, +20,$ and $+30°$. The zoom of Figure 4b shows that the LH histogram for $\lambda_{sc} \leq -10°$ (boldface) strongly peaks close to V = +1. This histogram also contains a large fraction of points with weaker polarization, and even a small bump between 0.2 and 0.5. Although some intrinsic SKR circular polarization ≤1 cannot be excluded, most of these low polarization measurements are due to the superposition of emissions from both hemispheres in the same pixel. We show below (section 8) that such a superposition is common up to λ_{sc}
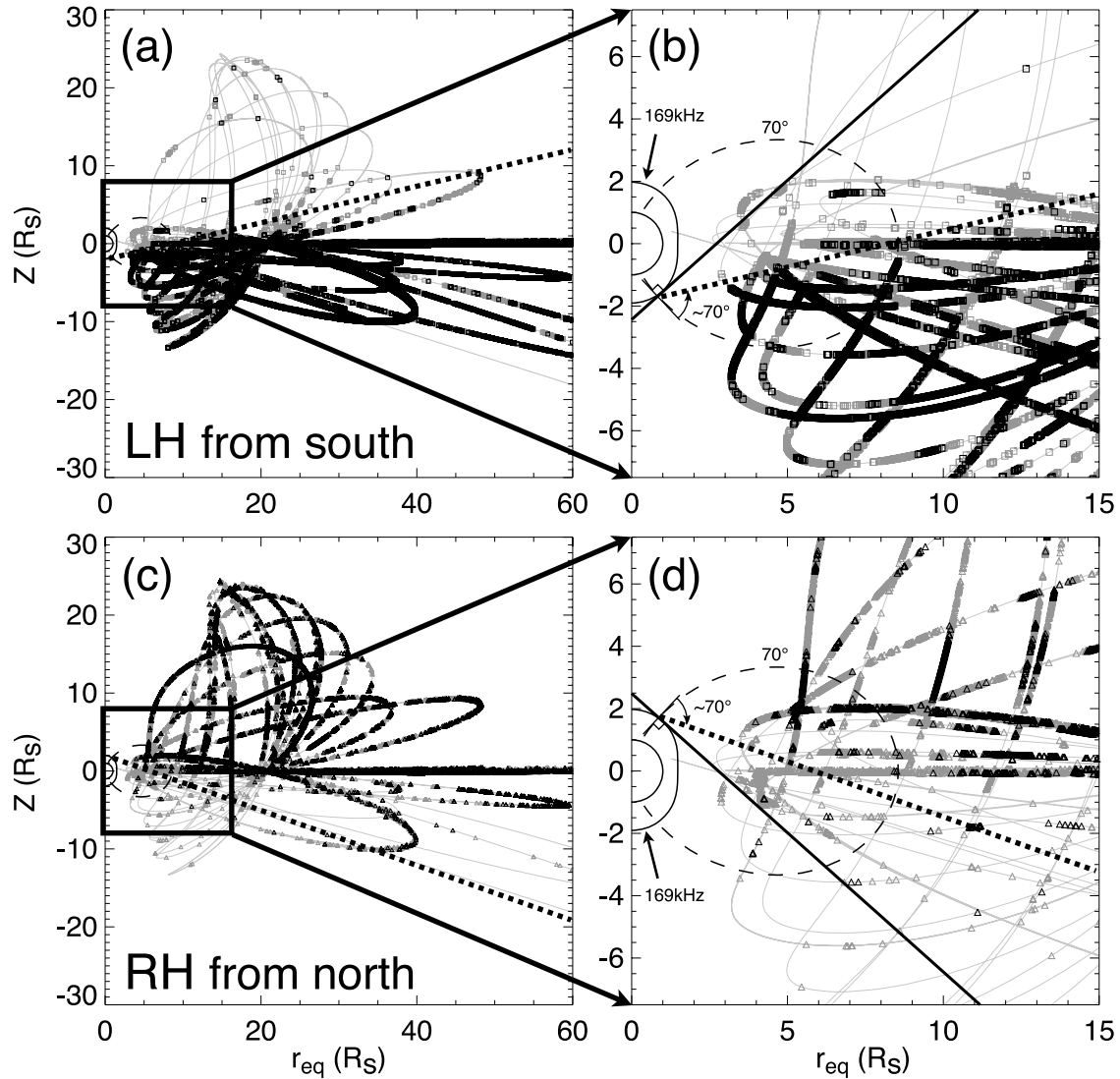
Figure 5. Highly polarized emissions ($|V| > 0.8$) at 169 kHz along Cassini's trajectory folded in a meridian plane. Black and grey symbols refer respectively to intense and weak events (above and below the median flux corresponding to the 50% detection level at that frequency). Figures 5a and 5b deal with LH polarization (squares) whereas Figures 5c and 5d deal with RH polarization (triangles). The dashed curve represents the magnetic field line of invariant latitude 70° (SPV field model [*Davis and Smith*, 1990]). The isocontour f_{ce} = 169 kHz is indicated by the thin black curve close to Saturn. The solid straight lines in Figures 5b and 5d are tangent to the f_{ce} = 169 kHz isosurface at its intersections with the 70° field line, which is the presumed position of the radio source. They also match well the equatorial limit of SKR detection. The dotted straight lines also originating from the presumed radio sources mark the observed equatorward limit of intense events, at $\sim$70° from the magnetic field direction in the source.

$\sim -20°$. For $\lambda_{sc} \leq -20°$ and $-30°$, the peak at V close to 1 persists, but the number of measurements rapidly decreases. To improve the determination of V, Figure 4b also displays LH histograms for $\lambda_{sc} \leq -10°$ with several SNR thresholds (lightface). As illustrated by the histogram corresponding to SNR $\geq$ 20 dB, this additional selection on SNR removes most of low polarization signals (including the bump between 0.2 and 0.5) whereas the right part of the histogram (highest V) is better defined. The 40 dB threshold leads to a peak at V = +0.99 ± 0.01.

[19] RH histograms also reveal a peak at V = -0.97 ± 0.03, but with a larger fraction of events with low circular polarization. However, observations from the northern hemisphere were performed mainly from Saturn's dusk side, where SKR is detected with a lower intensity. Also, as shown by *Cecconi and Zarka* [2005], the SNR directly influences the determination of V, with lower SNR implying lower apparent V (see Appendix and Figure A1). LH emissions, observed from the southern hemisphere mainly from the morning side, correspond to highest SKR intensities and thus to most significant values of V.

[20] Figures 4c and 4d investigate the possible detection of L-O mode emission. Latitudinal selections are consequently the opposite to those of Figures 4a and 4b, for the same polarization senses. A more severe limitation on λ_{sc} is also applied to minimize pollution by dominant R-X mode:
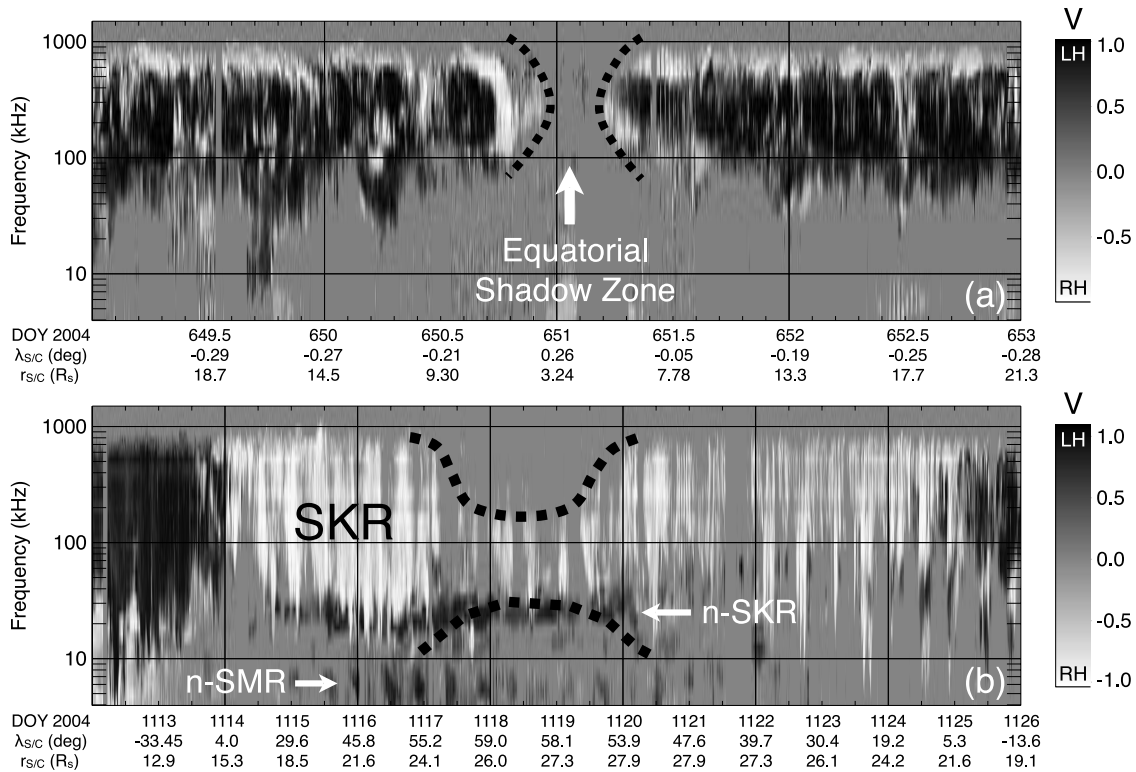
Figure 6. Dynamic spectra of the SKR circular polarization degree, quantified by the grey scale bar on the right-hand side of the plots. The spectra are shown for time intervals corresponding to an equatorial and a polar disappearance of the radio emission. (a) During the near-equatorial passage on DOY 649–653, containing the observation of a perikrone with closest approach at 3.01 R_s (DOY 651), SKR disappears during several hours at the crossing of the equatorial shadow zone, whose extent versus frequency is emphasized by the dashed thick lines. The equatorial extent of the shadow zone is minimum at 200 kHz, where it is about 4 R_s. It increases up to ∼6−7 R_s at 80 and 900 kHz. (b) During the northern pass on DOY 1113–1126, with λ_{sc} reaching 59.2° on DOY 1118, the upper (and to a lesser extent the lower) frequency ends of the SKR range disappear for $\lambda_{sc} > 55°$, as again emphasized by the dashed thick lines. The figure also shows the occurrence of n-SMR and n-SKR at low frequencies for high latitudes.

we use $\lambda_{sc} \leq -40°$ and SNR ≥ 20 dB for RH emissions (solid lines) and $\lambda_{sc} \geq 40°$ and SNR ≥ 20 dB for LH ones (dashed lines). Histogram counts are much lower than for Figures 4a and 4b, as expected for the weaker L-O mode possibly swamped in R-X mode emissions. Nevertheless, a peak is clearly detected for LH emissions at V = 1.00 ± 0.01 (see Figure 4d). This peak is consistent with either detection of L-O mode from the northern hemisphere, or observation of LH R-X mode apparently coming from the northern hemisphere, e.g., due to refraction in Saturn's complex plasma environment. Detailed source location and ray-tracing studies are beyond the scope of the present paper, but further evidence of L-O mode detection is discussed in section 8.

[21] The above results strongly support by direct polarization measurements the fact that X mode SKR is ∼100% circularly polarized. They justify a posteriori the use of the goniopolarimetric inversion described in the Appendix [see *Cecconi and Zarka*, 2005]. The predominance of R-X mode emissions is confirmed, but highly polarized emissions compatible with L-O mode are also detected. According

to these results, we will hereafter use a threshold of $|V_{lim}| = 0.8$ to define and select highly polarized events.

5. Beaming and Shadow Zones

[22] In Figure 5 we plotted the spacecraft positions, along Cassini's trajectory folded in a meridian plane, from where highly polarized SKR was detected at 169 kHz (close to the SKR peak). These plots confirm that LH emission is observed mainly from the south and RH from the north, consistent with dominant R-X mode. The solid straight lines tangent to the $f_{ce} = 169$ kHz isosurface also define the equatorial limits of SKR detection. Assuming that the radio beaming angle from the SKR sources may reach the maximum value of 90°, this suggests that SKR sources are located along field lines of invariant latitude $\geq 70°$. This is consistent with previous results obtained under various assumptions [*Kaiser et al.*, 1981; *Kaiser and Desch*, 1982; *Lecacheux and Genova*, 1983; *Galopeau et al.*, 1995]. Then, considering sources on a field line whose invariant latitude is 70°, the fact that the most intense SKR events (black symbols on Figure 5) are detected at $\leq 70°$ from the
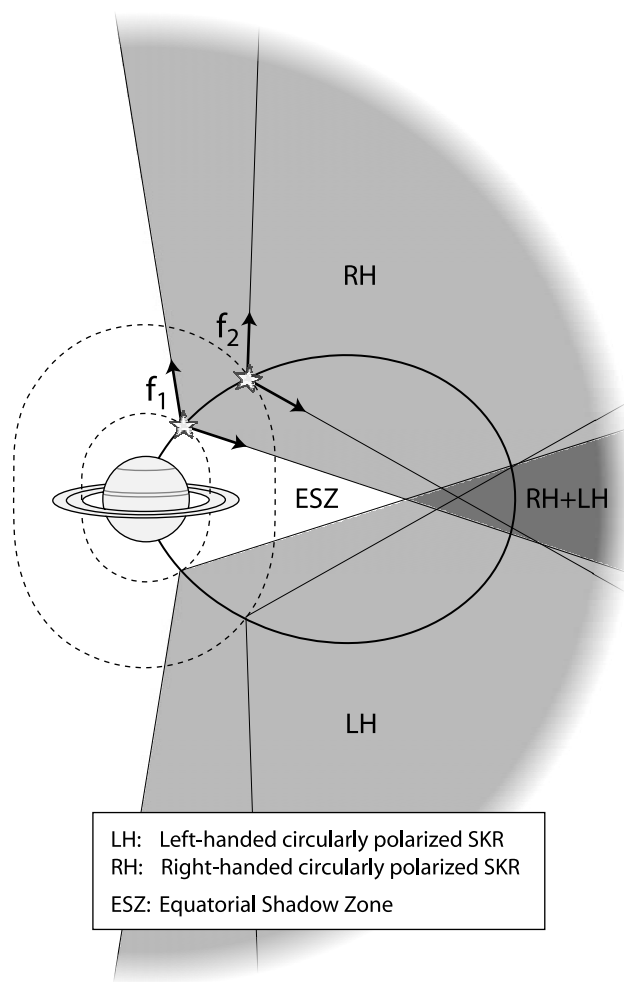
Figure 7. Sketch of the equatorial shadow zone generated by an anisotropic (hollow cone) radio beaming. Stars represent radio sources at two frequencies ($f_1 \geq f_2$) along the same magnetic field line (solid line). We assume both frequencies to be above 100 kHz in order to neglect refraction effects. The altitude of the sources is fixed by the magnetic field intensity, each source being at the intersection of the magnetic field line and of the isocontour corresponding to $f = f_{ce}$ (dashed lines). Radio emission is beamed along a hollow cone (black arrows). The possible 3D distribution of radio sources over a range of longitudes results is the filling of the shaded regions, but radio emission remains excluded from a near-equatorial shadow zone whose shape and extent depend on the detailed source locations and on the beaming angle as a function of frequency.

magnetic field direction suggests that the typical SKR beaming angle is $\leq 70°$. This statistical 2D view must be refined by 3D case studies, but a straightforward consequence is the existence of an equatorial shadow zone (qualitatively proposed by *Lecacheux and Genova* [1983]) where emission is not detected. We measure here its equatorial extension at 169 kHz: $r_{eq} \sim 4$ R_s.

[23] Figure 6 illustrates disappearances of the emission related to the spacecraft location. Figure 6a shows the crossing of the equatorial shadow zone during a perikrone (on DOY 651) with a closest approach at 3.01 R_s. The minimal equatorial extension of the shadow zone occurs for frequencies between 200 and 400 kHz at $r_{eq} \sim 4$ R_s. At 80 and 900 kHz, the shadow zone extent increases to $r_{eq} \sim 6{-}7$ R_s.

[24] In the above analysis we have neglected refraction effects that might affect radio wave propagation at Saturn. On the basis of an average plasma distribution model in the inner kronian magnetosphere (such as Figure 3 of *Galopeau et al.* [1989]), the iso-f_X surface at 100 kHz extends to ≤ 3 R_s from the planet, maximum extension being in the equatorial plane. Thus we don't expect significant refraction to occur for emission above ~ 100 kHz from a source at invariant latitude $\sim 70°$, even for a beaming angle reaching 90°. This justifies our first order assumption of straight line propagation. Figure 7 accordingly sketches how the anisotropic beaming of the radio emission generates equatorial shadow zones. The shadow zone extent varies with the frequency because of two factors: the position of the source along the field line (as shown on Figure 7) and possibly the aperture angle of the emission cone which may strongly decrease at high frequencies as modeled by *Galopeau et al.* [1989].

[25] Cassini measurements also revealed the systematic disappearance of SKR at high frequencies (and to a lesser extent at low frequencies) when the spacecraft latitude exceeds $\sim +55°$. Figure 6b displays an example of this signature observed during a high latitude northern flyby (dominant RH polarization observed). For $\lambda_{sc} \geq 55°$, emission disappears above 200 kHz and below 30 kHz. Dashed lines emphasize how SKR visibility varies with λ_{sc}. Extinction starts at both ends of the spectrum, and propagates to intermediate frequencies over a few degrees increase of λ_{sc}. This signature is not observed in the south, in spite of λ_{sc} reaching values as low as $-60°$. This is likely to be due to the different observing conditions of SKR during northern and southern high latitude passes: northern passes with $\lambda_{sc} \geq 55°$ occurred for Cassini located at $r_{sc} = [24,29]$ R_s and $LT_{sc} = [18,22]$ h, while southern ones ($\lambda_{sc} \leq -55°$) occurred at $r_{sc} = [9,16]$ R_s and $LT_{sc} = [6,10]$ h. Interpretation of SKR extinctions at high latitudes appears thus more complex than for the equatorial shadow zone, and deserves a 3D analysis that will be carried out in a follow-on paper dealing with modeling SKR visibility along Cassini's orbit.

6. Average Spectra and Power

[26] Figure 8 displays SKR flux density levels observed 50% (median), 10% and 1% (peak) of the time, as a function of frequency. LH and RH components are plotted separately. Figures 8a, 8c, and 8d, with a logarithmic frequency scale, emphasize the lower frequency part of the spectrum, while Figure 8b, with a linear scale, emphasizes the upper frequency part of the spectrum.

[27] Figures 8a and 8b focus on near-equatorial observations, with $|\lambda_{sc}| \leq 1°$. RH spectra of Figure 8a are remarkably similar to Voyager ones [*Kaiser et al.*, 1980]. SKR extends from ~ 10 to 1300 kHz and peaks between 100 and 400 kHz at about 7×10^{-19} Wm^{-2} Hz^{-1} for the 1% occurrence level. Figure 8b shows a linear decrease of the intensity above the SKR peak. Low frequency enhancement observed below 10 kHz is due to local emissions
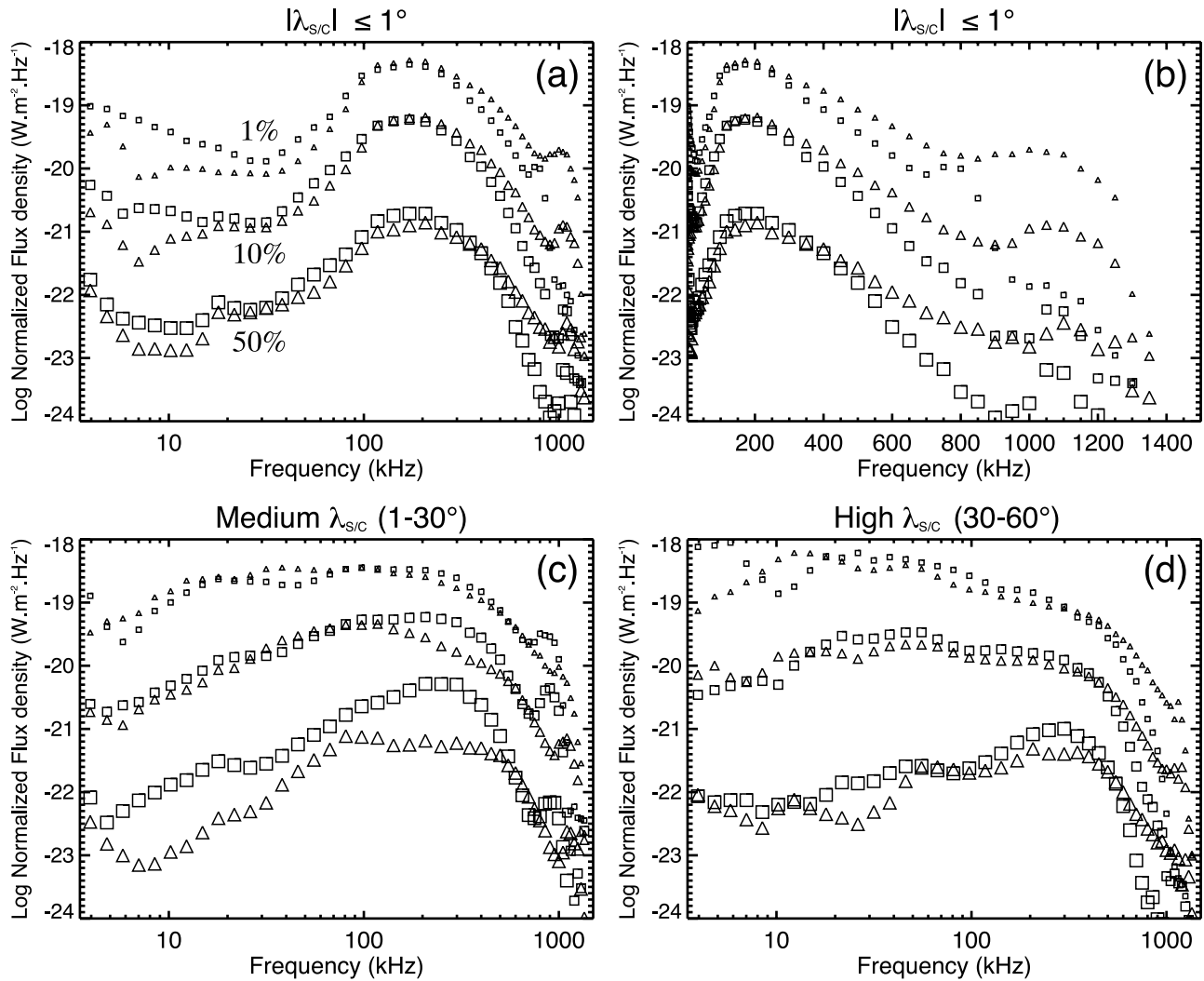
Figure 8. Occurrence levels of LH (squares) and RH (triangles) SKR as a function of frequency over our 2.75 years data set. The flux density levels, normalized to 1 AU, reached 50%, 10%, and 1% of the time are represented respectively as large, medium and small symbols. The median spectra (50% occurrence levels) are a very good proxy for average SKR spectra. Figures 8a and 8b focus on near-equatorial observations ($|\lambda_{sc}| \leq 1°$), Figure 8c on intermediate latitude observations ($-30° \leq \lambda_{sc} < -1°$ for LH and $1° < \lambda_{sc} \leq 30°$ for RH), and Figure 8d on high latitude observations ($-60° \leq \lambda_{sc} < -30°$ for LH and $30° < \lambda_{sc} \leq 60°$ for RH). The frequency scale is logarithmic in Figures 8a, 8c, and 8d, and linear in Figure 8b.

observed near perikrones. On both sides of the main peak, weaker secondary components are observed around 20 kHz and 1100 kHz. The low frequency component is not n-SMR or n-SKR since these emissions are mostly observed from high latitudes. LH and RH spectra are remarkably similar, except that RH spectra are more intense above 200 kHz, and extend to slightly higher frequencies (50 to 100 kHz) than LH ones. The latter feature, already mentioned about Figure 3b, is consistent with the 0.04 R_s offset of the kronian magnetic field toward the northern direction and/ or the presence of a magnetic anomaly more intense in the north [*Galopeau et al.*, 1992].

[28] Figure 8c displays spectra similar to those of Figure 8a, but for intermediate latitude observations: $-30° \leq \lambda_{sc} < -1°$ for LH emissions and $1° < \lambda_{sc} \leq 30°$ for RH ones (we thus mainly restrict to the dominant polarization in each

hemisphere; see sections 3 and 4). The main difference with spectra of Figure 8a is the stronger intensity level below 80 kHz. The LF part of the SKR spectrum now extends down to ∼3.5 kHz (the LF limit of the instrument). The faint high frequency secondary component is still observed but shifted to lower frequencies (between 800 and 1100 kHz). The spectral behavior of both polarizations remains similar except for the 50% occurrence level, which can be up to one order of magnitude more intense in LH polarization than in RH. This difference is again likely to be due to the different observing conditions of SKR in both hemispheres.

[29] Finally, Figure 8d focuses on high latitude observations: $-60° \leq \lambda_{sc} < -30°$ for LH emissions and $30° < \lambda_{sc} \leq 60°$ for RH ones. Compared to Figure 8c, the lower frequency part of the spectra is again increased while the upper frequency part is slightly less intense. The faint high

Table 1. Total Radiated LH and RH Powers Per Steradian (in $W \cdot sr^{-1}$), Integrated Between 3.5 and 1500 kHz

Occurrence Probability	50%	10%	1%
LH	2.7×10^7	4.8×10^8	3.3×10^9
RH	1.5×10^7	4.6×10^8	3.9×10^9

frequency secondary component is no more apparent, and LH and RH spectra are quasi-identical. The shift of SKR spectrum toward low frequencies when the latitude of the observer increases corresponds to the detection of sources located at higher altitudes. The high frequency component (at 800–1100 kHz) deserves further study, with special care to be taken of the possible pollution by spacecraft interference lines observed at multiples of 100 kHz over the whole RPWS/HFR range.

[30] The total radiated LH and RH powers, integrated between 3.5 and 1500 kHz (see computation in the Appendix), corresponding to the above 50%, 10% and 1% occurrence levels, are listed in Table 1. As the solid angle corresponding to the integrated radio beaming pattern is not precisely known, we chose to express radiated powers per unit solid angle (i.e., in $W \cdot sr^{-1}$). Radiated power values are similar for both polarizations, with a difference of a factor

~2 at the 50% occurrence in favor of LH power. This point is discussed in section 7.

7. Temporal Variations

[31] Figure 9 addresses variations of LH and RH SKR power as a function of time. On Figures 9a and 9b, the LH and RH radiated powers have been integrated over the 100–400 kHz bandwidth and smoothed using a 1-day sliding window. The displayed interval (DOY 620 to 930) corresponds to near-equatorial orbits ($|\lambda_{sc}| \leq 1°$), that provide quasi-identical observing conditions for both polarizations. Over this interval, LH and RH powers have similar magnitudes, varying between a few $MW \cdot sr^{-1}$ and ~1 $GW \cdot sr^{-1}$. Computing a linear cross-correlation [see *Bevington and Robinson*, 1992] over both time series averaged to obtain a time resolution of 1 day, we measure a coefficient C ≥ 80%. When using the original time series of radiated powers, at 3 min time resolution, instead of the averaged ones, the correlation is reduced to C ~40%. In both cases, maximum correlation is obtained for a zero time lag, and the confidence level on C (=1 minus the probability to get the same correlation coefficient with two random data sets of same length) is very close to 100%, thus correlation is highly significant.
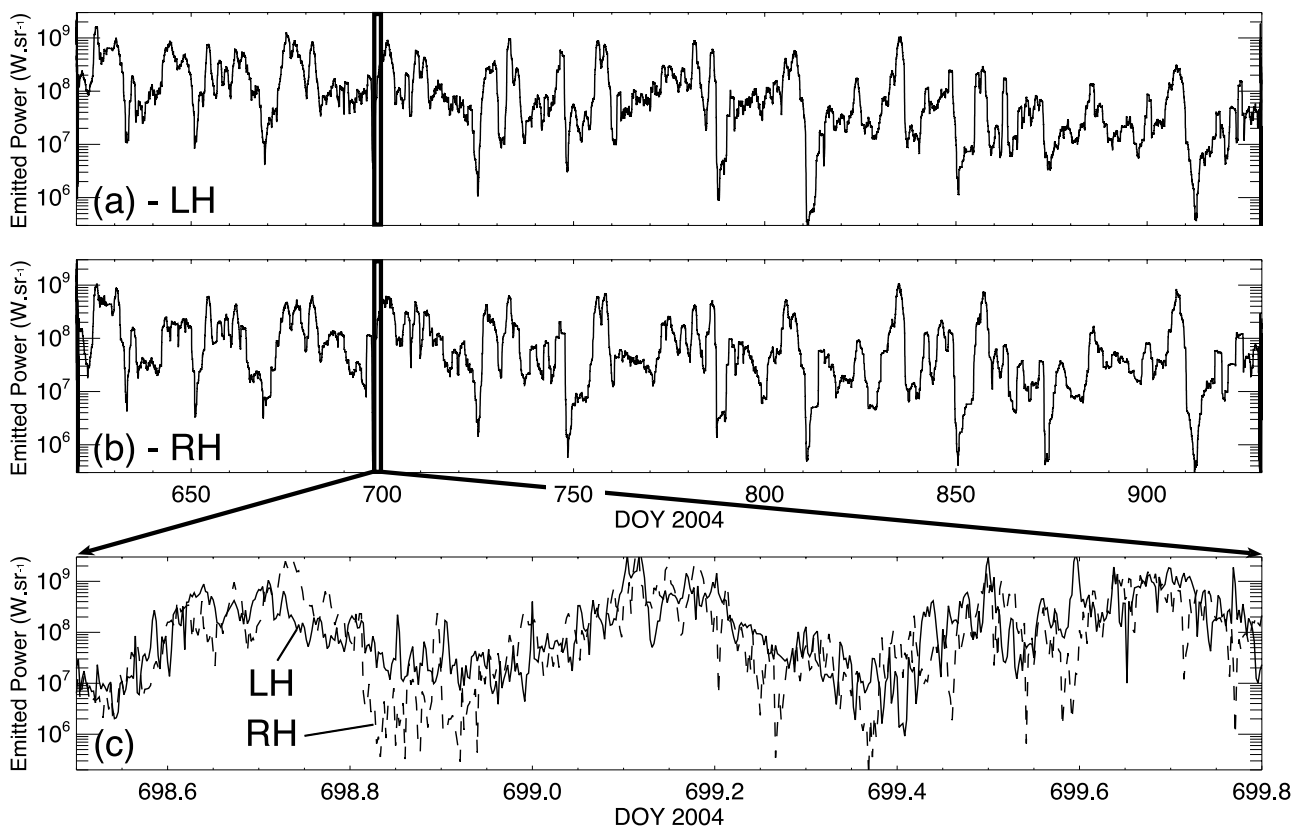

Figure 9. Total power radiated by each polarized component between 100 and 400 kHz (expressed in $W \cdot sr^{-1}$). Figures 9a and 9b display LH and RH powers smoothed over 1 day between DOY 620 and 930. This interval corresponds to near-equatorial orbits ($|\lambda_{sc}| < 1°$) when observing conditions of LH and RH polarizations were similar. Figure 9c shows a zoom around DOY 699 where LH (solid) and RH (dashed) powers are superimposed, at the full time resolution of 3 min.
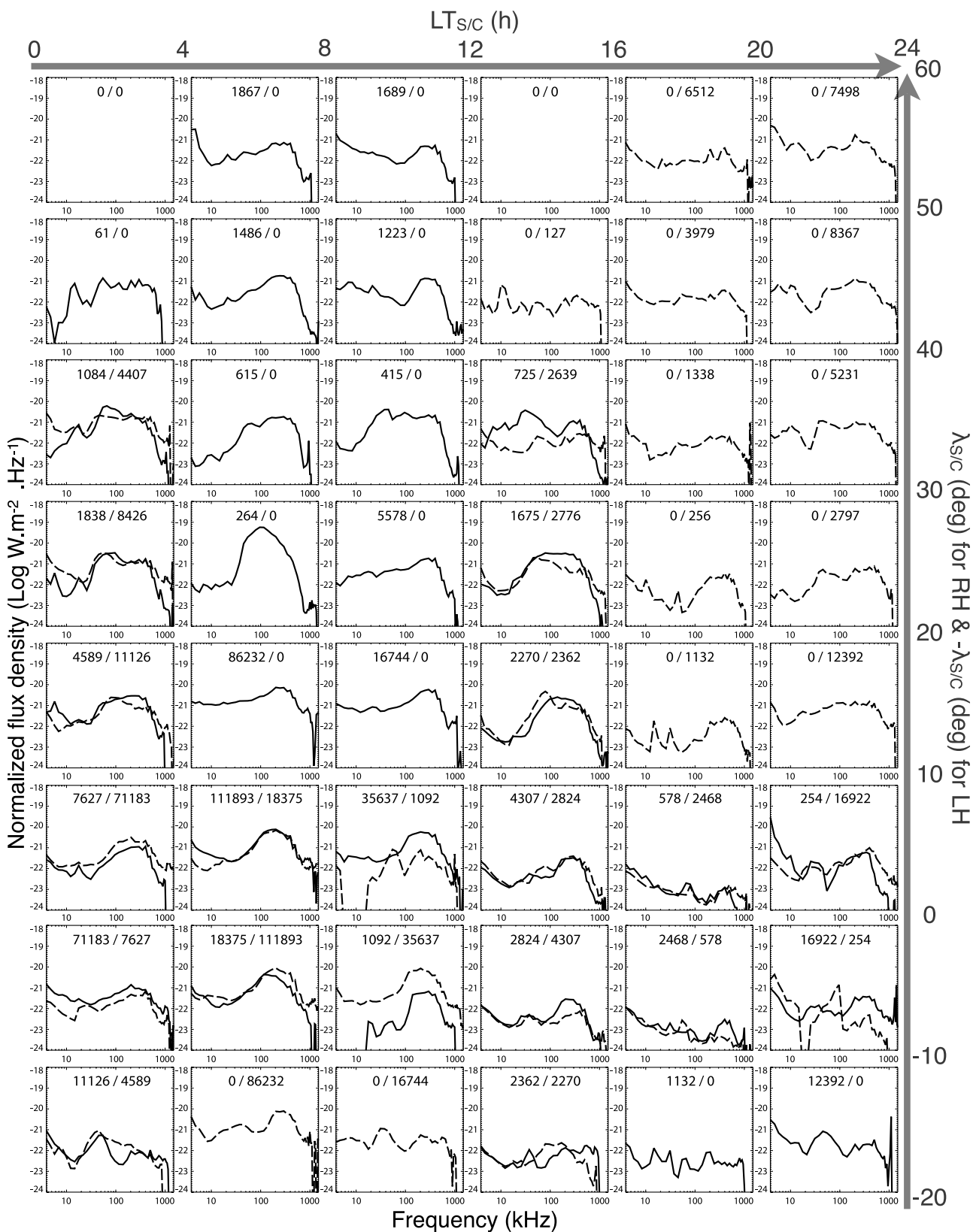
Figure 10. Median flux density spectra over our 2.75 years data set sorted by local time and latitude of the observer. The 50% occurrence spectra of LH (solid) and RH (dashed) SKR are plotted within intervals of 4 h of LT_{sc} by 10° of λ_{sc}. RH spectra for a given interval of λ_{sc} are superimposed to LH spectra for the same interval of $-\lambda_{sc}$. The two numbers at the top of each panel are the number of individual (3 min) LH and RH SKR spectra involved in the computation of the median.
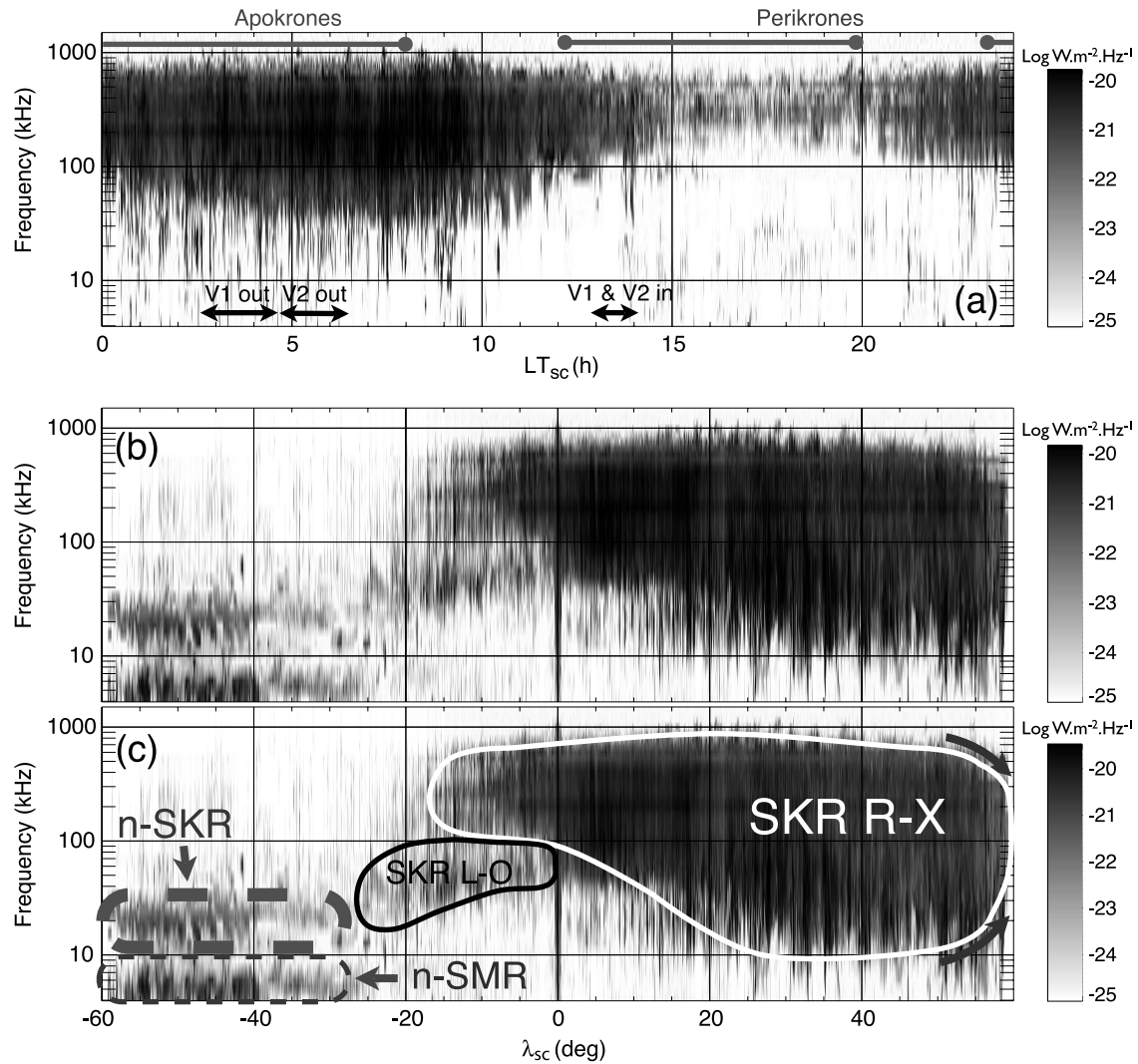
Figure 11. Dynamic spectra of flux density, normalized to one AU distance of observer, reached by 50% of the highly circularly polarized ($|V| > 0.8$) SKR events. (a) SKR intensity versus LT_{sc} and frequency, computed from near-equatorial observations ($|\lambda_{sc}| \leq 1°$). Ranges of LT explored by the Voyager spacecraft are indicated by black double arrows. (b, c) SKR intensity versus λ_{sc} and frequency, computed from all available data over 2.75 years. Figure 11c is identical to Figure 11b, with the addition of contours emphasizing the various components identified on the dynamic spectrum. R-X dominant SKR corresponds to the white contour, n-SMR and n-SKR to the dashed grey contours. The black contour indicates an LF component detected between $-25°$ and $0°$ of latitude, whose characteristics are compatible with L-O mode emission, and which has a visibility different from R-X mode.

[32] Figure 9c investigates in more detail the temporal conjugacy of LH and RH power series at a shorter timescale (3 min) over a representative interval of $\sim$30 h. During this interval, 3 broad maxima of SKR power are detected, corresponding to a modulation at or close to the planetary rotation period [*Zarka et al.*, 2007]. Computing the cross-correlation between the two time series after averaging the data over consecutive intervals of duration δt, we found that the correlation coefficient increases from C $\leq$ 0.1 with δt = 3 min, to C $\geq$ 0.5 with δt = 30 min, and C $\sim$ 0.7−0.8 with $\delta t \geq$ 1 h. A similar result has been obtained previously by *Zarka* [1988]. However, as Cassini detects both components simultaneously from low latitudes, the power of LH and RH components compete for detection so that resulting

power series are necessarily more noisy when time resolution decreases. Thus the lower correlation coefficient for lower δt does not necessarily imply that LH and RH variations are less correlated at short timescales. We conclude that LH and RH powers are strongly conjugated at timescales $\geq$30 min, and possibly also at shorter timescales. We did not measure any significant variation of this conjugacy as a function of LT_{sc}.

[33] LH power is also found, over the interval displayed on Figures 9a and 9b, to be larger than RH one by a factor varying between one and three. This is consistent with the trend observed in previous sections: dominant polarization in Figure 3b, 50% occurrence level spectrum in Figures 8a and 8b, and average power at 50% occurrence level in

Table 1. Although corresponding to near-equatorial observations, all show dominant LH polarization between 100 and 400 kHz. This difference in favor of LH emissions may be related to a seasonal effect. During the 2.75 years studied, the subsolar latitude is about $-18°$. Saturn's southern hemisphere is thus more exposed to the Sun and the solar wind than the northern one. This might affect in a different way (still to be determined) the spectrum of the auroral radio emission originating from each hemisphere, as it was observed for the AKR at Earth [*Green et al.*, 2004].

8. Spectral Dependence on λ_{sc} and LT_{sc}, SKR Visibility and O-Mode Emission

8.1. Spectral Dependence on λ_{sc} and LT_{sc}

[34] Figure 10 shows the 50% occurrence spectra of LH (solid) and RH (dashed) SKR, within intervals of 4 h of LT_{sc} by 10° of λ_{sc}. RH spectra for a given interval of λ_{sc} are superimposed to LH spectra for the same interval of $-\lambda_{sc}$. Intervals corresponding to $\lambda_{sc} \leq -20°$ contain almost no data and are thus not shown. Intensities are larger on Saturn's dawn side. The weakest emission levels are observed between 16 h and 20 h LT_{sc}. Figure 10 also reveals important variations with λ_{sc}, with maximum SKR intensity and frequency extent being observed between 20° and 40°. We find that whenever there are enough data in any (LT_{sc}, λ_{sc}) bin, RH (LT_{sc}, λ_{sc}) and LH $(LT_{sc}, -\lambda_{sc})$ average spectra are nearly identical. This confirms that SKR sources behave similarly in both hemispheres, and suggests that the consistent LH and RH spectral variations with respect to LT_{sc} and λ_{sc} are not noise fluctuations but directly relate to source location and beaming. Thus we can add together LH $(LT_{sc}, -\lambda_{sc})$ and RH (LT_{sc}, λ_{sc}) spectra in order to study global variations of SKR as a function of LT_{sc} or λ_{sc}.

8.2. SKR Visibility

[35] Restricting to near-equatorial orbits $(|\lambda_{sc}| < 1°)$ in order to avoid variations of visibility depending on λ_{sc}, we can analyze separately the SKR visibility as a function of LT_{sc}, for which Cassini provided a full coverage. Figure 11a displays the median SKR intensity versus LT_{sc} and frequency. Intense events with a broad spectrum are preferentially observed when the spacecraft is located between 02 h and 11 h LT_{sc}. This range is consistent with radio sources located on Saturn's morning side, but also with the LT domain where Cassini was at apokrone. The range of Cassini perikrones similarly matches that of minimum SKR activity in Figure 11a. This correspondence suggests that an observational bias may be present since most of the perikrones on the dusk side occurred at distances below ~ 5 R_s, thus probably in the equatorial shadow zone (see section 5). However, the study of an equatorial orbit at the end of year 2006 (DOY 912 to 936), with a quasi-symmetrical coverage of dawn and dusk sides and a perikrone at $LT_{sc} \sim 12$ h, shows that SKR is still preferentially observed from the morning side, with maximum intensity and bandwidth between 02 h and 08 h LT_{sc}. The above observational bias is therefore at most partial. More observations from the dusk side are required to derive an unbiased distribution corresponding to Figure 11a.

[36] Latitudinal exploration by Cassini is more homogeneous. Taking advantage of the conjugacy revealed by Figure 10 between RH (LT_{sc}, λ_{sc}) and LH $(LT_{sc}, -\lambda_{sc})$ spectra, we add them together to study on Figures 11b and 11c how SKR intensity and bandwidth vary with λ_{sc}. Most of the SKR is observed between $-20°$ and at least 60° (white contour in Figure 11c). This dominant emission has a polarization consistent with the R-X mode. Bandwidth is maximum for λ_{sc} between 25° and 50°.

8.3. O-Mode Emission

[37] The low frequency emissions below $-20°$ have been identified as n-SMR and n-SKR (dashed grey contours) in section 3. Faint emissions between ~ 100 and 400 kHz at a latitude below $-40°$ have a polarization consistent with L-O mode, but they are generally swamped in R-X mode of opposite polarization. However, other weak emissions with polarization consistent with L-O mode show up more clearly in the band between 20 and 100 kHz at latitudes between $-25°$ and 0° (black contour), clearly distinct from the region of detection of n-SMR and n-SKR. These weak emissions have a circular polarization degree as high as dominant R-X mode emissions (i.e., from the same hemisphere), but of opposite sign, and an intensity at least one order of magnitude lower than R-X mode emissions. These emissions are detected at each value of $|\lambda_{sc}|$ at frequencies below the LF limit of dominant R-X mode emissions. In addition, goniopolarimetric analysis of these emissions indicates that they preferentially come from the hemisphere where Cassini is located at the time of detection. This makes their interpretation as refracted R-X mode from the opposite hemisphere unlikely. The best interpretation for the origin, polarization, intensity, and frequency range of these emissions is thus in terms of L-O mode emission.

9. Conclusions

[38] Extensive data collected by the Cassini-RPWS/HFR instrument over 2.75 years starting at Cassini's Saturn orbit insertion allowed us to derive average and statistical properties of SKR.

[39] The broadband SKR is not the only emission observed by RPWS-HFR. We discussed the distinct narrowband electromagnetic component in the range $\sim 10-40$ kHz, that we called here n-SKR. Both the n-SKR and the n-SMR (below 20 kHz) are preferentially observed from high latitudes. They are modulated at or close to the SKR rotational periodicity. Both of them are circularly polarized but the circular polarization of n-SKR is higher whereas its intensity is weaker than that of the n-SMR.

[40] We confirmed Voyager results about the SKR spectrum, extending from a few kHz to 1200 kHz (with a peak between 100 and 400 kHz), with R-X mode emission being largely dominant. We obtained the first direct evidence that the circular polarization degree of SKR reaches 100%. In addition we showed that Cassini probably detected weaker L-O mode emissions. Goniopolarimetric analyzes confirmed that X-mode SKR detected with RH (resp. LH) polarization comes from the northern (resp. southern) hemisphere. RH emission extends to higher frequencies than LH one, which is consistent with Saturn's northward magnetic field offset and/or magnetic anomaly.

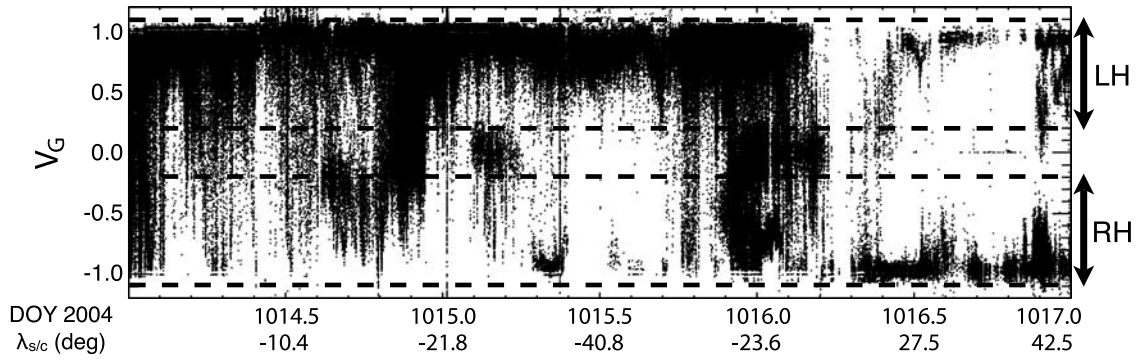[41] Focusing on highly polarized events, we found that SKR sources are likely to be confined to latitudes $\geq 70°$.

Figure A1. Normalized degree of circular polarization V_G provided by Goniometric inversion between DOY 1014 and 1017. Only data points with an SNR higher than 25 dB are plotted. Dashed lines indicate the ranges selected to recognize SKR ($-1.1 < V_G < -0.2$ for RH and $0.2 < V_G < 1.1$ for LH emission) while rejecting most of the spurious points. The sign of dominant values of V_G changes along with λ_{sc}.

The typical beaming angle of sources at $f \sim f_{ce} = 169$ kHz located along field lines with an invariant latitude of $70°$ is estimated to be $\leq 70°$. This beaming results in the existence of an equatorial radio shadow zone. We detected it and measured its extent as a function of frequency. This extent is minimum for frequencies between 200 and 400 kHz ($r_{eq} \sim 4$ R_s). At 80 and 900 kHz, it increases to $r_{eq} \sim 6-7$ R_s. We also discovered high latitude SKR extinctions for $\lambda_{sc} > 55°$, whose interpretation is more tricky than in the equator and deserves a 3D analysis of SKR source location and beaming.

[42] Typical radiated power for X-mode SKR is in the range $10-100$ $MW \cdot sr^{-1}$. LH power (and average spectra between 100 and 400 kHz) is found to be systematically more intense than RH one. This feature is possibly due to a seasonal effect. LH and RH intensity variations are found to match together at all timescales ≥ 30 min, and perhaps at shorter timescales.

[43] We found that LH and RH spectra are conjugate with respect to λ_{sc}. This allowed us to add together both polarizations versus $\pm \lambda_{sc}$ in order to derive the average variations of SKR visibility. Prominent variations of the SKR intensity and bandwidth are observed as a function of both LT and latitude of the observer. SKR is observed from all local times but more intense on the morning side. Part of this asymmetry between the dawn and dusk sides is probably related to the inhomogeneous LT coverage by Cassini and requires further investigation that will be possible when the dusk side of the magnetosphere will be thoroughly explored. Emission characteristics also strongly depend on the spacecraft latitude. Dominant R-X mode is observed down to $-20°$ (relative to the RH latitude reference) with a maximum frequency extent between $25°$ and $50°$. L-O mode is possibly detected between 100 and 400 kHz below $-40°$, and more certainly below 100 kHz between $-25°$ and $0°$, where it is not swamped in R-X mode SKR.

[44] The strong variations reported here of SKR visibility with the observer's position will be the input of a subsequent modeling study (based on the CMI theory), intending to explain the detailed observations and bring tight con-

straints on SKR sources localization and parameters of the generated emission (beaming angle, etc.).

Appendix A: Processing of Cassini-RPWS/HFR Data

[45] The Cassini-RPWS/HFR instrument onboard Cassini performed radio observations in many operating modes, with different integration times, frequency resolution and scale, and using two (one dipole + one monopole) or three (monopoles) electric antennas. Electromagnetic and electrostatic emissions as well as RFI are detected altogether in the dynamic spectra produced by the instrument. The aim of the data processing pipeline described here is to create a clean database of circularly polarized electromagnetic emissions, thus containing mainly SKR. This database consists of dynamic spectra of calibrated fluxes (in $W \cdot m^{-2} \cdot Hz^{-1}$) normalized to 1 AU, circular polarization degrees, **SNR (in dB)** and time series of radiated powers (in $W \cdot sr^{-1}$).

A1. Selection of Antenna Measurement Type

[46] RPWS/HFR is able to perform two or three antenna measurements providing respectively four or seven auto- and cross-correlations. *Cecconi and Zarka* [2005] developed direct analytical inversions to be applied to radio data recorded by the HFR experiment. These inversions provide the physical parameters of the received electromagnetic waves: the four Stokes parameters (S, Q, U and V [*Kraus*, 1966]) and the wave direction of arrival (azimuth θ and colatitude ϕ). It is possible to retrieve the 6 wave parameters with three-antenna measurements, whereas no more than 4 wave parameters can be retrieved from two-antenna measurements. During the 2.75 years interval studied in this paper, 92.6% of the data have been recorded in two-antenna mode (dipole X and monopole Z) and 7.4% in three-antenna mode (monopoles). We consequently produced long-term data series from two-antenna measurements only (three-antenna measurements can each be processed as two consecutive two-antenna measurements). With adequate
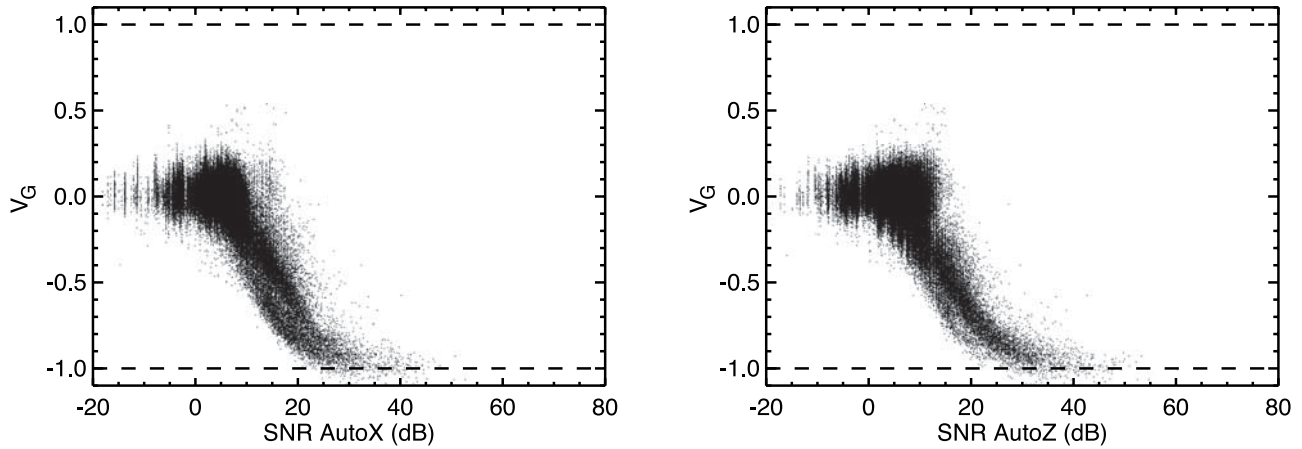
Figure A2. Normalized degree of circular polarization V_G provided by Goniometric inversion for DOY 1100 (predominant RH SKR, i.e., V_G close to -1) as a function of SNR of autocorrelation measured on each antenna (dipole X and monopole Z). Only data points corresponding to frequencies above 100 kHz are considered to avoid low-frequency n-SKR emissions. A selection is also applied on the geometric configuration between sources and the antennas plane ($\beta \geq 20°$ following *Cecconi and Zarka* [2005]). Both images show that highest SNR match highest V_G.

assumption on 2 of the 6 wave parameters, the two-antenna measurement inversions provide the four remaining ones.

[47] Beyond $r_{sc} \sim 150\ R_s$ (before SOI), the angular size of Saturn as seen from Cassini was $\leq 0.75°$, which is smaller than the goniopolarimetric accuracy of $1°$ to $2°$. The radio sources in Saturn's environment can then be considered to be located along the direction of Saturn's center. Taking the coordinates of Saturn's center (θ, ϕ) as fixed source coordinates, the "Polarimetric" inversion of *Cecconi and Zarka* [2005] (hereafter noted P) provides the intensity S_P, the normalized degree of circular polarization V_P and the normalized degrees of linear polarization U_P and Q_P. Since the start of the Cassini tour of Saturn in July 2004, we cannot anymore assume that the radiosources lie in the direction of Saturn's center. However, *Cecconi and Zarka* [2005] also showed from pre-SOI data that the SKR linear polarization degrees are close to 0. Assuming no linear polarization, the "Goniometric" inversion (hereafter noted G) extracts the intensity S_G, the normalized degree of circular polarization V_G and the direction of arrival of the waves (θ_G, ϕ_G). For the interval studied in this paper, starting near SOI, the Goniometric inversion is the most relevant.

A2. Selection of SKR

[48] The sign of V_G allows us to discriminate between the two polarized components of SKR: LH polarization corresponds to $V_G > 0$ and RH polarization to $V_G < 0$. Figure A1 shows that the observed values of V_G oscillate between ~ -1 and ~ 1.

[49] *Cecconi and Zarka* [2005] showed that the accuracy on V_G (or V_P) measurements mainly depends on both the SNR and the geometric configuration between the wave direction and the antennas plane. Figure A2 thus illustrates that highest SNR correspond to highest V_G.

[50] *Cecconi and Zarka* [2005] also estimated the typical uncertainty on V_G about 0.1, leading to occasionally observed values of $|V_G|$ larger than 1 (see Figures A1 and A2).

Consequently, we define the following range of polarization to select SKR: $0.2 < |V_G| < 1.1$.

[51] The selection using V_G removes most of electrostatic and solar emissions as well as part of the RFI, but some frequency bands remain polluted in particular by harmonics of 100 kHz which corresponds to the operating frequency of many power converters onboard Cassini. To further reduce the pollution by these RFI, we apply an additional selection using V_P with the same ranges as the ones defined for V_G. As RFI affect differently each computation of V_G and V_P, this double selection results in a more efficient cleaning of the data and a better selection of SKR. Figure A3 illustrates how RFI bands disappear thanks to a joint (V_G, V_P) selection.

A3. Creation of Long-Term Series

[52] Data tagged as LH or RH SKR are then processed separately to produce long-term series organized in regular arrays of frequencies and times. These final arrays require fixed time resolution and spectral scale. The time resolution depends on the maximal sweeping time of the whole HFR frequency range, which is about 90 s [cf. *Gurnett et al.*, 2004]. Following *Zarka et al.* [2004], we chose here a time resolution equal to 180 s. We also chose a relatively coarse frequency ramp defined by 24 logarithmically spaced channels between 3.5 and 300 kHz (with $\Delta f/f = 20\%$) and 24 linearly spaced channels between 350 and 1500 kHz (with $\delta f = 50$ kHz).

A4. Initial Integration

[53] As RPWS/HFR operates in a large variety of modes, data are first processed mode per mode. For each operating mode, data are first integrated in initial regular arrays whose time ramp has a resolution equal to 180 s (at Saturn, including light time travel correction) and whose spectral scale corresponds to that of the mode considered. S_G and
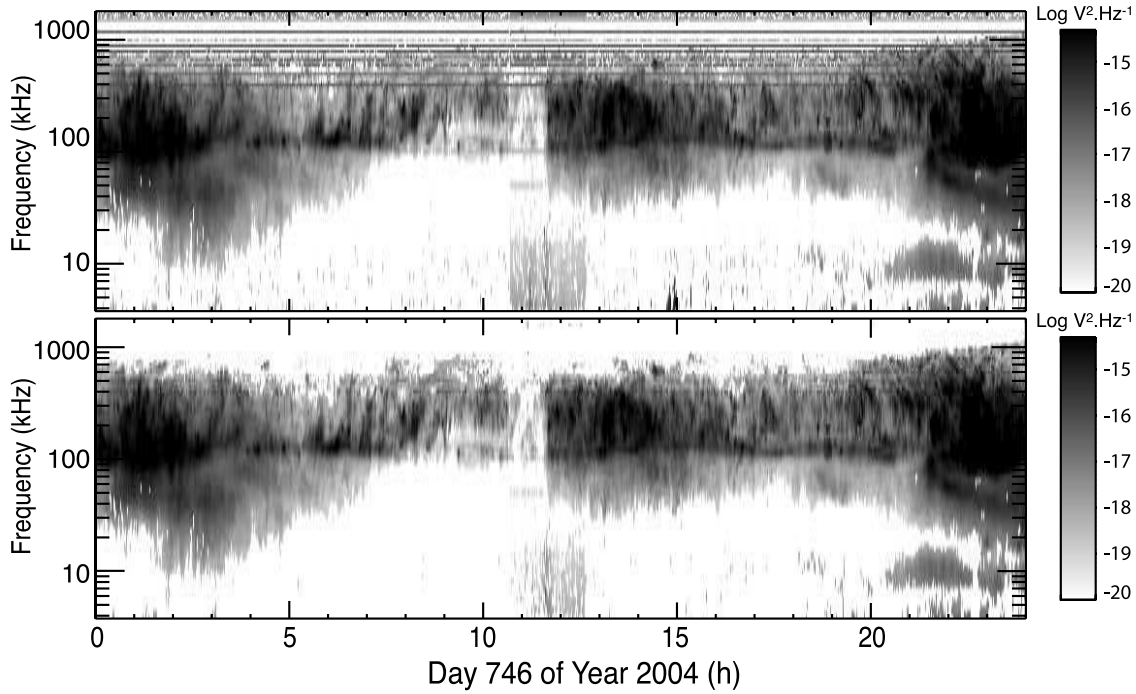
Figure A3. Dynamic spectra of the flux density S_G expressed here in $V^2 \cdot Hz^{-1}$ for DOY 746. Figure 14a displays the data selected by the condition $0.2 < |V_G| < 1.1$, while Figure 14b displays the data selected by the conditions $0.2 < |V_G| < 1.1$ and $0.2 < |V_P| < 1.1$. The latter choice is more efficient at removing RFI (horizontal lines at multiples of 100 kHz) and local electrostatic emissions (e.g., about 15 h). The spectra are reinterpolated (in frequency) after RFI suppression.

V_G corresponding to measurements for which $-0.2 < |V_G| < 0.2$ or $-0.2 < |V_P| < 0.2$ are set to 0.

[54] Fluxes S_G in $V^2 \cdot Hz^{-1}$ are transposed into fluxes S_W in $W \cdot m^{-2} \cdot Hz^{-1}$ following [*Zarka et al.*, 2004]:

$$S_W = \frac{S_G}{Z_0 \left(\frac{LC_a}{C_a + C_b} \right)^2} \qquad (A1)$$

where Z_0 is the impedance of free space $\sim 377\ \Omega$, L the effective length of the RPWS monopole $\mathbf{h}_z \sim 1.68$ m, C_a and C_b the antenna and base capacitances with $C_a/(C_a + C_b) \sim 0.4$.

[55] $SNR_{X,Z}$ refer to SNR of autocorrelation measured on each antenna (dipole X and monopole Z) expressed in dB. We consequently take into account two SNR values for each two-antenna measurement.

[56] Then S_i, P_i, V_i and $SNR_{X,Z,i}$ (hereafter SNR_i) arrays are filled following an averaging scheme that takes into account weighting by the integration time and frequency bandwidth of original measurements. If each array element corresponds to m time steps and n frequencies of original ($S_{Wm,n}$, $V_{Gm,n}$, $SNR_{X,Z,m,n}$) data sets, and (*) refers to the polarization selection (LH or RH):

$$S_i(*) = \frac{\Sigma_{m,n} S_{Wm,n}(*) \delta t_m(*) \delta f_n(*)}{\Sigma_m \delta t_m \Sigma_n \delta f_n} \qquad (A2)$$

$$P_i(*) = \frac{\Sigma_{m,n} S_{Wm,n}(*) \delta t_m(*) \delta f_n(*)}{\Sigma_m \delta t_m(*)} \qquad (A3)$$

$$V_i(*) = \frac{\Sigma_{m,n} V_{Gm,n}(*) S_{Wm,n}(*) \delta t_m(*) \delta f_n(*)}{\Sigma_{m,n} S_{Wm,n}(*) \delta t_m(*) \delta f_n(*)} \qquad (A4)$$

$$SNR_i(*) = \frac{\Sigma_{m,n} SNR_{X,Z,m,n}(*) S_{Wm,n}(*) \delta t_m(*) \delta f_n(*)}{\Sigma_{m,n} S_{Wm,n}(*) \delta t_m(*) \delta f_n(*)} \qquad (A5)$$

Power P_i differs from flux S_i by an integration on the spectral bandwidth and a temporal averaging only over selected emission (*). Equations (A4) and (A5) are weighted by flux densities to take into account that the polarization of intense events should not be artificially reduced by that of adjacent low intensity events.

A5. RFI Elimination

[57] The cleaning step is applied only on S_i and P_i arrays (V_i and SNR_i arrays retain the initial information). For each spectrum, we remove isolated pixels to exclude frequencies possibly polluted by residual RFI with $|V_i| \geq 0.2$. Then, as the typical frequency width of interference lines removed by the selection step is about $2-3$ pixels, we fill-in missing frequencies by linear interpolation over non-null values of the spectrum, only when the number of consecutive null pixels is lower than 4. We checked that this interpolation maximizes spectral continuity without adding significant artificial signal.

A6. Final Integration

[58] Final S_f, P_f, V_f and SNR_f arrays are filled by values of the initial arrays after RFI elimination and spectral

interpolation, using again equations (A2), (A3), (A4), and (A5). If the final spectral scale is of higher resolution than the frequency ramp of the current mode, an additional interpolation is applied on S_f and P_f arrays. Data gaps are identified by affecting the default unphysical value -1 to S_f and P_f arrays, whereas the V_f and SNR_f arrays are filled with the value 0. Data gaps represent 7.6% of the 2.75 years interval studied.

A7. Received Flux

[59] Dynamic spectra of calibrated fluxes (in $W \cdot m^{-2} \cdot Hz^{-1}$) normalized to 1 AU are obtained after inverse-square correction from the distance from Cassini to Saturn:

$$S = S_f \times r_{au}^2 \qquad (A6)$$

where r_{au} is the Cassini-Saturn distance in Astronomical Units.

A8. Radiated Power

[60] The average total radiated power P_W (expressed in W) emitted by the radio sources over a given frequency range $[f_{min}, f_{max}]$ can be written as:

$$P_W = \Omega \times r^2 \int S_W(f)\, df \qquad (A7)$$

where S_W is the flux density in $W \cdot m^{-2} \cdot Hz^{-1}$, r the distance to Saturn in m, Ω the solid angle of the overall emission beam. As the radio beaming is anisotropic and the corresponding solid angle of the emission unknown, we rather compute $P = P_W / \Omega$ expressed in $W \cdot sr^{-1}$.

[61] Thus time series of radiated power P are directly obtained from final P_f arrays by integrating over a bandwidth $[f_{min}, f_{max}]$ and by correcting from distance following:

$$P = \int P_f \times r^2 df \qquad (A8)$$

where r is the distance to Saturn in m.

[62] A typical example showing the effect of this processing on Cassini-RPWS/HFR radio data is displayed on Figure 2.

References

Bevington, B. V., and D. K. Robinson (1992), *Data Reduction and Error Analysis for the Physical Sciences*, pp. 198–200, McGraw-Hill, New York.

Cecconi, B., and P. Zarka (2005), Direction finding and antenna calibration through analytical inversion of radio measurements performed using a system of 2 or 3 electric dipole antennas, *Radio Sci.*, 40, RS3003, doi:10.1029/2004RS003070.

Cecconi, B., P. Zarka, and W. S. Kurth (2006), SKR polarization and source localization with the Cassini/RPWS/HFR instrument: First results, in *Planetary Radio Emissions*, vol. VI, edited by H. O. Rucker, W. S. Kurth, and G. Mann, pp. 37–49, Austrian Acad. Sci., Graz, Austria.

Davis, L., Jr., and E. J. Smith (1990), A model of Saturn's magnetic field based on all available data, *J. Geophys. Res.*, 95, 15,257–15,261.

Galopeau, P. H. M., and A. Lecacheux (2000), Variations of Saturn's radio rotation period measured at kilometer wavelengths, *J. Geophys. Res.*, 105, 13,089–13,102.

Galopeau, P., P. Zarka, and D. Le Queau (1989), Theoretical model of Saturn's kilometric radiation spectrum, *J. Geophys. Res.*, 94, 8739–8755.

Galopeau, P., P. Zarka, and A. Ortega-Molina (1992), Reply to comment on "Evidence of Saturn's magnetic field anomaly from Saturnian kilometric radiation high-frequency limit", *J. Geophys. Res.*, 97, 12,291–12,297.

Galopeau, P. H. M., P. Zarka, and D. Le Quéau (1995), Source location of Saturn's kilometric radiation: The Kelvin-Helmholtz instability hypothesis, *J. Geophys. Res.*, 100, 26,397–26,410.

Green, J. L., S. Boardsen, L. Garcia, S. F. Fung, and B. W. Reinisch (2004), Seasonal and solar cycle dynamics of the auroral kilometric radiation source region, *J. Geophys. Res.*, 109, A05223, doi:10.1029/2003JA010311.

Gurnett, D. A., W. S. Kurth, and F. L. Scarf (1981), Narrowband electromagnetic radiation from Saturn's magnetosphere, *Nature*, 292, 733–737.

Gurnett, D. A., et al. (2004), The Cassini radio and plasma wave science investigation, *Space Sci. Rev.*, 114(1–4), 395–463.

Hilgers, A. (1992), The auroral radiating plasma cavities, *Geophys. Res. Lett.*, 19, 237–240.

Kaiser, M. L., and M. D. Desch (1982), Saturnian kilometric radiation: Source location, *J. Geophys. Res.*, 87, 4555–4559.

Kaiser, M. L., M. D. Desch, J. W. Warwick, and J. B. Pearce (1980), Voyager detection of nonthermal radio emission from Saturn, *Science*, 209, 1238–1240.

Kaiser, M. L., M. D. Desch, and A. Lecacheux (1981), Saturnian kilometric radiation: Statistical properties and beam geometry, *Nature*, 292, 731.

Kaiser, M. L., M. D. Desch, W. S. Kurth, A. Lecacheux, F. Genova, B. M. Pedersen, and D. R. Evans (1984), Saturn as a radio source, in *Saturn*, Space Science Series, edited by T. Gehrels and M. S. Matthews, pp. 378–415, Univ. Arizona Press, Tucson, Ariz.

Kraus, J. D. (1966), *Radio Astronomy*, pp. 116–125, McGraw-Hill, New York.

Lecacheux, A., and F. Genova (1983), Source localization of Saturn kilometric radio emission, *J. Geophys. Res.*, 88, 8993–8998.

Le Quéau, D., R. Pellat, and A. Roux (1985), The maser synchrotron instability in an inhomogeneous medium application to the generation of the auroral kilometric radiation, *Ann. Geophys.*, 3, 273–291.

Louarn, P., and D. Le Quéau (1996a), Generation of the auroral kilometric radiation in plasma cavities. Part I: Experimental study, *Planet. Space Sci.*, 44, 199–210.

Louarn, P., and D. Le Quéau (1996b), Generation of the auroral kilometric radiation in plasma cavities. Part II: The cyclotron maser instability in small size sources, *Planet. Space Sci.*, 44, 211–224.

Louarn, P., et al. (2007), Observation of similar radio signatures at Saturn and Jupiter, implications for the magnetospheric dynamics, *Geophys. Res. Lett.*, 34, 20,113, L20113, doi:10.1029/2007GL030368.

Mutel, R. L., W. M. Peterson, T. R. Jaeger, and J. D. Scudder (2007), Dependence of cyclotron maser instability growth rates on electron velocity distributions and perturbation by solitary waves, *J. Geophys. Res.*, 112, A07211, doi:10.1029/2007JA012442.

Ortega-Molina, A., and A. Lecacheux (1990), Polarization response of the Voyager-PRA experiment at low frequencies, *Astron. Astrophys.*, 229, 558–568.

Treumann, R. A. (2000), Planetary radio emission mechanisms: A tutorial, in *Radio Astronomy at Long Wavelengths*, edited by R. G. Stone et al., 13 pp., AGU, Washington, D. C.

Warwick, J. W., et al. (1981), Planetary radio astronomy observations from Voyager 1 near Saturn, *Science*, 212, 239–243.

Warwick, J. W. (1982), Planetary radio astronomy observations from Voyager 2 near Saturn, *Science*, 215, 582–587.

Wu, C. S., and L. C. Lee (1979), A theory of the terrestrial kilometric radiation, *Astrophys. J.*, 230, 621–626.

Zarka, P. (1988), Beaming of planetary radio emissions, in *Planetary Radio Emissions II*, edited by H. O. Rucker, S. J. Bauer, and B. M. Pedersen, pp. 327–342, Austrian Acad. Sci. Press, Vienna.

Zarka, P. (1998), Auroral radio emissions at the outer planets: Observations and theories, *J. Geophys. Res.*, 103, 20,159–20,194.

Zarka, P., B. Cecconi, and W. S. Kurth (2004), Jupiter's low-frequency radio spectrum from Cassini/Radio and Plasma Wave Science (RPWS) absolute flux density measurements, *J. Geophys. Res.*, 109, A09S15, doi:10.1029/2003JA010260.

Zarka, P., L. Lamy, B. Cecconi, R. Prangé, and H. O. Rucker (2007), Modulation of Saturn's radio clock by solar wind speed, *Nature*, 450, 265–267.

───────────────

B. Cecconi, L. Lamy, R. Prangé, and P. Zarka, LESIA, Observatoire de Paris, CNRS, UPMC, Université Paris Diderot, 5 Place Jules Janssen, 92190 Meudon, France. (laurent.lamy@obspm.fr)

D. A. Gurnett and W. S. Kurth, Department of Physics and Astronomy, University of Iowa, Iowa City, IA 52242, USA.